Fluid Phase Equilibria 570 (2023) 113798

Contents lists available at ScienceDirect

Fluid Phase Equilibria

journal homepage: www.journals.elsevier.com/fluid-phase-equilibria

Multi-scale modeling of gas solubility in semi-crystalline polymers: bridging Molecular Dynamics with Lattice Fluid Theory

Omar Atiq [a,b], Eleonora Ricci [a,b,1], Marco Giacinti Baschetti [a,b], Maria Grazia De Angelis [a,b,c,*]

[a] Department of Civil, Chemical, Environmental and Material Engineering, (DICAM), Alma Mater Studiorum – Università di Bologna, via Terracini 28, Bologna 40131, Italy
[b] Dutch Polymer Institute (DPI), P.O. Box 902, 5600 AX, Eindhoven, the Netherlands
[c] Institute for Materials and Processes, School of Engineering, University of Edinburgh, Sanderson Building, Robert Stevenson Road, Scotland EH9 3FB, United Kingdom

ARTICLE INFO

Keywords:
Gas solubility
Semicrystalline polymers
Molecular modeling
Multiscale modeling
Equation of state

ABSTRACT

The prediction of the solubility of gasses in semi-crystalline polymers is still a challenging task due to the difficulty in providing a comprehensive description of the morphological and mechanical perturbation felt by the amorphous phase intercalated with the impermeable crystal domains. Among the different modeling techniques, a frequently adopted strategy models the reduced solubility experienced by the confined amorphous phase via an additional pressure to the external gas pressure acting on the latter, the so-called constraint pressure 'p_c'. The work presented here is dedicated to a newly developed multi-scale modeling strategy, belonging to the aforementioned category, that innovatively couples Molecular Dynamics simulations with Lattice Fluid theory. The model was applied to carbon dioxide, ethylene, and propane solubility isotherms in High-Density Polyethylene, and validated against experimental literature data, confirming its ability to model the solubility in semi-crystalline polymers. In addition, it showed good accordance with a fully macroscopic model already present in the literature. The successful multi-scale coupling presented here paves the way for the development of a fully predictive modeling strategy.

1. Introduction

In the last decades, polymers have acted as main characters in a wide array of applications, ranging from common usage to high-performance services. Although several classifications of such materials exist, a noticeable one relies on their morphology, which is deeply related to key macroscopic features. Semi-crystalline polymers, in this regard, are biphasic materials that, instead of having a fully random coil chains architecture, as pure amorphous polymers, incorporate ordered domains called crystallites. Upon cooling from the melt, once the degree of supercooling overcomes the crystal nuclei-amorphous interfacial free energy, a part of the randomly distributed chains begins to self-fold and align forming lamellar structures. After nucleation, according to the applied stress tensor and temperature time and space gradients, groups of lamellae developing from distinct nucleation centers build up into a series of complex crystalline domains differing in amount, dimension, and shape [1–3]. At the end of the crystallization, the residual uncrystallized molten mass remains in the amorphous state. Nevertheless, tight intercalation with the crystal phase is guaranteed by an articulated population of chains that is continuously flowing across the interface, providing the material with a unique topology as depicted in Fig. 1.

The existence of the crystal phase is responsible for outstanding features. The intermolecular interactions holding adjacent chains packed in the lamellae provide them with enhanced ability to withstand stresses, hence limiting the matrix deformation, also in the amorphous domains [4–6]. In addition, tie chains and entanglements improve mechanical resistance by acting as stress transmitters between the connected crystal domains. Moreover, the semi-crystalline morphology provides excellent gas barrier properties [7–12]. The Permeability across dense materials, according to the solution-diffusion model [13], is the product of the Solubility and Diffusivity coefficients, which are both strongly affected by the presence of the crystallites. Compared to a

* Corresponding author at: Institute for Materials and Processes, School of Engineering, University of Edinburgh, Sanderson Building, Robert Stevenson Road, Scotland EH9 3FB, United Kingdom.
E-mail address: Grazia.deangelis@ed.ac.uk (M.G. De Angelis).
[1] Current address: Institute of Informatics and Telecommunications & Institute of Nanoscience and Nanotechnology, National Center for Scientific Research "Demokritos", Patr. Grigoriou E' and 27 Neapoleos St., 15341, Aghia Paraskevi, Athens, Greece.

https://doi.org/10.1016/j.fluid.2023.113798
Received 12 December 2022; Received in revised form 19 February 2023; Accepted 9 March 2023
Available online 12 March 2023

wholly amorphous polymer volume, the experimental solubility of the semi-crystalline materials is drastically reduced, primarily because the crystal phase does not adsorb. On top of that, the amorphous phase fraction itself generally shows a lower fluid solubility compared to the wholly amorphous one; that is conventionally ascribed to the interaction with the crystal phase, that alters the morphological and volumetric properties of the amorphous region [14–18].

At the same time, the diffusion coefficient is decreased in reason of the tortuosity generated by the impermeable crystal domains; nevertheless, the reduced amorphous free volume and chain mobility also represent a non-negligible contribution [19–23].

Many authors have addressed the topic of fluid solubility in semi-crystalline polymers and developed different modeling techniques [24], but there is still the need to improve their predictive power and transferability. The strategies present in the literature rely on a fully amorphous phase model in which the crystal-induced perturbation is taken into account from different perspectives.

A class of models considers the fraction of elastically effective chains 'f' (active tie-chains) to be responsible for the reduced swelling of the amorphous matrix, hence introducing an additional elastic term to the Equation of State (EoS) chemical potential that is a function of f, which is treated as a model adjustable parameter [18,25,26].

Another relevant class of models, instead, embodies the overall crystal effect on a fictitious constraint pressure 'p_c', that is added to the gas pressure acting on the polymer phase. In this framework, Memari et al., relying on a fully amorphous molecular structure, modeled the solubility of gasses in polyethylene below the melting temperature by adding such a constraint pressure parameter and fitting it to match the Monte Carlo simulated solubility with the experimental reference [27,28]. Some years later, Minelli et al. transferred the concept of the additional constraint pressure at a fully macroscopic level (Lattice Fluid theory [29]) by introducing the latter as an adjustable parameter in the Sanchez-Lacombe EoS [30]. More recently, Fischlschweiger et al. aimed at boosting the predictive ability of the strategy by deriving an expression for the constraint pressure that was directly linked with the EoS specific volume through the material elastic constants and the mass degree of crystallinity [31]. A detailed explanation of the different available modeling techniques can be found in our previous review article dedicated to the topic [24].

Following these considerations, the present work introduces a modeling strategy belonging to the category of 'additional constraint pressure (p_c)' models, which aims at improving the precision and flexibility of previous models through the adoption of a multi-scale approach. From this point of view, because of the adopted atomistic and macroscopic coupling, the present model figures as a hybrid version of those proposed by Memari et al. and Minelli et al. The choice of using a multi-scale strategy came from the idea of exploiting the in-depth depiction provided by the atomistic description of gas-polymer systems without the load of time-consuming phase equilibrium simulations, which is delegated to the fast response of the thermodynamic model.

2. Modeling

2.1. Molecular modeling

High-density polyethylene (HDPE) amorphous phase molecular structure was represented with three all-atom linear chains having 443 monomers each ($M_w = 12{,}406$ g/mol), leading to a total number of 7980 atoms . The choice for such a simplified molecular model will be extensively addressed in Section 3.1.

The chains were inserted simultaneously with the Amorphous Builder tool of the Materials and Processes Simulations (MAPS) software by Scienomics accounting for non-bonded interactions. The initial simulation cubic box edge was 42.6 Å. Both the polymer and penetrant molecules (carbon dioxide, ethylene, and propane) bonded and non-bonded interactions were modeled with PCFF, a class II force field [32] provided by LAMMPS [33]. A graphical representation of all the potential energy contributions accounted for in the force field functional form is schematically reported in Table S1 in the *Supporting Information*. Intramolecular interactions potential expressions comprise a quartic polynomial for each bond stretching (Eq. (1)) and angle bending (Eq. (2)) and a three-term Fourier expansion for dihedral angles torsional contributions (Eq. (3)). Out-of-plane angles are computed according to Wilson [34] (Eq. (4)).

$$U_{Bonds} = \sum_{i=1}^{N_{Bonds}} b_{i,2}\left(r - r_{0,i}\right)^2 + b_{i,3}\left(r - r_{0,i}\right)^3 + b_{i,4}\left(r - r_{0,i}\right)^4 \quad (1)$$

$$U_{Angles} = \sum_{i=1}^{N_{Angles}} a_{i,2}\left(\Theta - \Theta_{0,i}\right)^2 + a_{i,3}\left(\Theta - \Theta_{0,i}\right)^3 + a_{i,4}\left(\Theta - \Theta_{0,i}\right)^4 \quad (2)$$

$$U_{Torsion} = \sum_{i=1}^{N_{Torsion}} \sum_{n=1}^{3} k_{i,n}\left(1 + \cos\left(n\ \Phi_i - \Phi_{0,\ i,n}\right)\right) \quad (3)$$

$$U_{\ Out-of-plane} = \sum_{i=1}^{N_{Wilson}} k_i\left(\chi - \chi_{0,i}\right)^2 \quad (4)$$

Second- and third-order cross-term expressions, quantifying the interplay between different contributions, such as Bond-Bond, Bond-Angle, Angle-Angle-Torsion, and others were not reported here for the

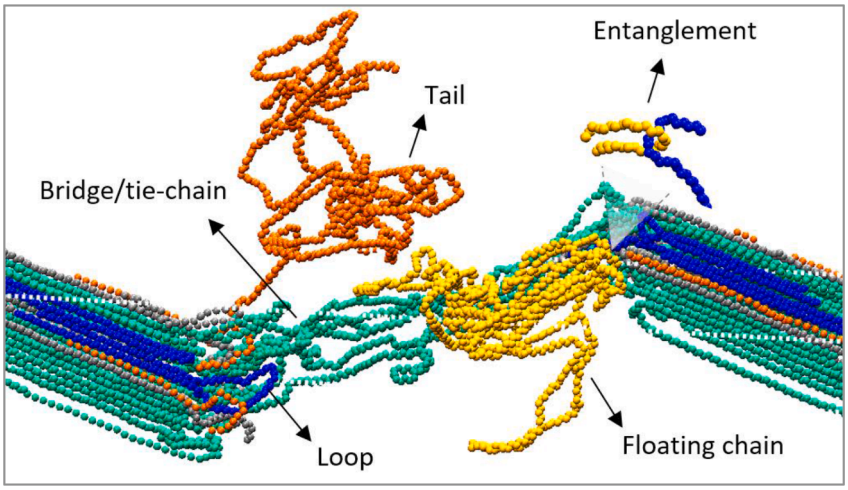

Fig. 1. Representation of a semi-crystalline material topology.

sake of synthesis. Nonetheless, the complete force field functional form and parameters can be found in Refs. [32,35].

On the other hand, non-bonded interactions were described using the LAMMPS *lj/class2/coul/long* pair style. The functional expression describing the Van de Waals interactions, together with its parameters, is chosen at the force field parametrization stage, and since it proved to be accurate for the aims of the present work, it was not changed from its original formulation. A 9–6 Lennard Jones pair potential expression therefore quantified the dispersion interactions (Eq. (5)) with a sixth-power mixing rule (Eq. (6)) and a cutoff distance r_c of 12 Å.

$$U_{LJ} = \frac{1}{2}\sum_{i,j=1}^{N_{Atoms}} \varepsilon_{ij}\left[2\left(\frac{\sigma_{ij}}{r_{ij}}\right)^9 - 3\left(\frac{\sigma_{ij}}{r_{ij}}\right)^6\right] \quad r_{ij} < r_c \tag{5}$$

$$\left.\begin{aligned}\sigma_{ij} &= \left(\frac{\sigma_i^6 + \sigma_j^6}{2}\right)^{\frac{1}{6}} \\ \varepsilon_{ij} &= \frac{2\sqrt{\varepsilon_i\varepsilon_j}\sigma_i^3\sigma_j^3}{\sigma_i^6 + \sigma_j^6}\end{aligned}\right\} \tag{6}$$

where ε_{ij} and σ_{ij} represent, respectively, the depth of the potential well and the distance at which the potential is zero, while r_{ij} is the distance between atom i and j.

Electrostatic interactions were described with Coulomb's law (Eq. (7)) for distances within the cutoff, whereas long-range interactions were computed in k-space using a particle-particle-mesh solver [36].

$$U_{Elect} = \frac{1}{2}\sum_{i,j=1}^{N_{Atoms}} \frac{Cq_iq_j}{\varepsilon r_{ij}} \quad r_{ij} < r_c \tag{7}$$

where the C term is an energy-conversion constant, q_i and q_j are the charges on the two atoms, and ε is the dielectric constant. A collection of PCFF force field parameters used for non-bonded interactions is reported in Table 1. End-chain and middle-chain carbon atoms are indicated as 'C3' and 'C2' respectively.

2.1.1. Simulation details

Molecular Dynamics (MD) simulations were performed to obtain pressure-volume-temperature data of molten amorphous HDPE, both pure and in the presence of penetrants. The simulations also provided an extrapolation of the theoretical unconfined amorphous system behavior below the melting temperature at pressures of 0.1, 40, and 80 MPa. Simulations were set up with 3D periodic boundary conditions. The initial velocities ensemble was created using a randomly generated Gaussian distribution at the specified temperature having zero linear and angular momentum. Newton's equations of motion were integrated with a time step of 1 fs while configuration recording was carried out every 1000 fs. Simulation temperature and pressure were controlled by a Nose-Hoover type thermostat and barostat with a damping factor of 10 and 150, respectively. Stress tensor diagonal components (hydrostatic pressure) were coupled ('iso' *command*) in NPT simulations.

Table 1
Non-bonded interactions PCFF force field parameters used in this work [32].

Molecule	σ (Å)	ε (kcal/mol)	q (e)
HDPE			
C2	3.367	0.062	−0.1060
C3	3.367	0.062	−0.1590
H	2.514	0.023	0.0530
Propane			
C2	3.367	0.062	−0.1060
C3	3.367	0.062	−0.1590
H	2.514	0.023	0.0530
Ethylene			
C	3.407	0.064	−0.2536
H	2.514	0.023	0.1268
Carbon-dioxide			
C	3.420	0.068	0.8000
O	2.935	0.067	−0.4000

The amorphous HDPE molecular structure previously defined was initially simulated in the NPT ensemble at $T_1 = 250$ °C and $P = 0.1$ MPa for 5 ns. After stabilization, the structure was cooled down to ambient temperature according to the following simulation path: for $i = 1{:}9$

1) NPT Temperature ramp from T_i to T_{i+1}, $P = 0.1$ MPa (200 ps)
2) NVT at T_{i+1} (50 ps)
3) NPT at T_{i+1} and $P = 0.1$ MPa (750 ps)

where $T_{i+1} = T_i - \Delta T$ with $\Delta T = 25$ °C.

Specific Volume versus Temperature data points were obtained by averaging simulation outputs at point 3) at each T_i.

At the same time, to obtain the stabilized configurations at 40 and 80 MPa and $T = 250$ °C, the simulated structure at $T_1 = 250$ °C and $P = 0.1$ MPa underwent a secondary simulation pathway that is here reported:

a) NPT at $T = 250$ °C, Pressure ramp from $P = 0.1$ MPa to $P = 40$ MPa, (2 ns)
b) NPT at $T = 250$ °C and $P = 40$ MPa (5 ns)
c) NPT at $T = 250$ °C, Pressure ramp from $P = 40$ MPa to $P = 80$ MPa, (2 ns)
d) NPT at $T = 250$ °C and $P = 80$ MPa (5 ns)

The stabilized configurations at the end of step b) and d) were afterwards simulated according to the first simulation pathway at the relative pressures, as for the case at 0.1 MPa, thus providing us also with the PVT data at 40 and 80 MPa.

Binary mixtures of penetrant in amorphous HDPE were simulated by building four initial configurations for each penetrant type, differing for the number of penetrant molecules inserted in the matrix, namely: 22, 35, 70, and 140 (210 for ethylene). Each configuration was stabilized at $T = 250$ °C and 0.1 MPa and simulated according to the previously reported pathways, thus allowing us to map the polymer partial density as a function of the penetrant mass fraction from 250 °C to 25 °C in the pressure range 0.1–80 MPa for each penetrant

It is important to stress that, at temperatures below the melting point, the simulated pressure in the simulation covers the meaning of an overall pressure felt by the matrix, encompassing the gas phase hydrostatic pressure and the fictitious constraint pressure mimicking the crystals confinement effect.

2.2. Thermodynamic modeling

At the macroscopic level, both the amorphous HDPE and gas molecules were modeled according to the Lattice Fluid theory [37]. In this framework, the Sanchez-Lacombe equation of state (EoS) was used for the modeling of single compounds pressure-volume-temperature data. The Sanchez-Lacombe EoS formalism for a pure compound is synthesized in Table S2 in the *Supporting Information*.

Pure CO_2 Sanchez-Lacombe EoS parameters (T^*, p^*, ρ^*) were taken from Ref. [38], whereas pure HDPE, ethylene, and propane parameters were regressed by using a least square minimization approach. HDPE and ethylene minimized objective function is the one reported in Eq. (8), namely, the sum of the square relative errors of the modeled compound specific volume with respect to the experimental one. Experimental molten pressure-volume-temperature data in the range 140–270 °C and 0.1–80 MPa were chosen for HDPE from Ref. [39], while gas-phase P-V-T data in the range 26.85–176.85 °C and 0.1–100 MPa were selected for ethylene [40]. Concerning propane, parameters were regressed by fitting L-V equilibrium data from [40] using the objective function reported in Eq. (9).

$$f(\boldsymbol{T}^*,\boldsymbol{p}^*,\boldsymbol{\rho}^*)=\sum_{i=1}^{N_T}\sum_{j=1}^{N_P}\left(\frac{\widehat{V}^{S-L}(\boldsymbol{T}^*,\boldsymbol{p}^*,\boldsymbol{\rho}^*,T_i,P_j)-\widehat{V}^{exp}(T_i,P_j)}{\widehat{V}^{exp}(T_i,P_j)}\right)^2 \tag{8}$$

$$f(\boldsymbol{T}^*,\boldsymbol{p}^*,\boldsymbol{\rho}^*)=\sum_{i=1}^{N_T}\left(\left(\frac{\widehat{V}_{LS}^{S-L}(\boldsymbol{T}^*,\boldsymbol{p}^*,\boldsymbol{\rho}^*,T_i,P_i^*)-\widehat{V}_{LS}^{exp}(T_i,P_i^*)}{\widehat{V}_{LS}^{exp}(T_i,P_i^*)}\right)^2+\left(\frac{\widehat{V}_{VS}^{S-L}(\boldsymbol{T}^*,\boldsymbol{p}^*,\boldsymbol{\rho}^*,T_i,P_i^*)-\widehat{V}_{VS}^{exp}(T_i,P_i^*)}{\widehat{V}_{VS}^{exp}(T_i,P_i^*)}\right)^2\right) \tag{9}$$

The Lattice Fluid formalism was employed also for the modeling of penetrant–amorphous polymer mixture, allowing to estimate the solubility by equating the chemical potential of the penetrant in the gas phase and in the polymer. Binary mixtures phase equilibria according to Lattice Fluid theory are reported in Table S3 of the *Supporting Information*. The LF formalism applies to the phase equilibria of a penetrant gas in a fully rubbery amorphous matrix; therefore, it can be directly applied to model sorption in the molten polymer. Nevertheless, as already pointed out, the modeling of the solubility isotherms in the confined amorphous phase below the melting point is performed by adding the fictitious constraint pressure (p_c) to the hydrostatic gas pressure (p_i), to account for the constraint effect. The term that is essentially modified is the penetrant reduced pressure in the amorphous phase:

$$\widetilde{p}_i=\frac{p_i+p_c}{p_i^*} \tag{10}$$

It is relevant to notice that the reduced pressure explicitly appears in the expression of the penetrant chemical potential of the gas in the confined amorphous polymer phase.

To obtain the solubility in the semi-crystalline polymer, ω_i^{sc}, and compare it with the experimental values below the melting transition, the modelled equilibrium penetrant mass fraction in the constrained amorphous phase, ω_i^{am}, needs to be rescaled by means of the mass degree of crystallinity (X_c), as follows:

$$\omega_i^{sc}=\omega_i^{am}(1-X_c) \tag{11}$$

The approach described so far represents the fully thermodynamic modeling strategy adopted by Minelli et al. [30]. The multi-scale modeling strategy here presented follows the same formalism, although relying on MD simulation derived P-V-T data of the penetrant-polymer mixture instead of describing them according to the S-L EoS.

2.3. Multi-scale modeling

As anticipated in the previous paragraphs, the multi-scale modeling

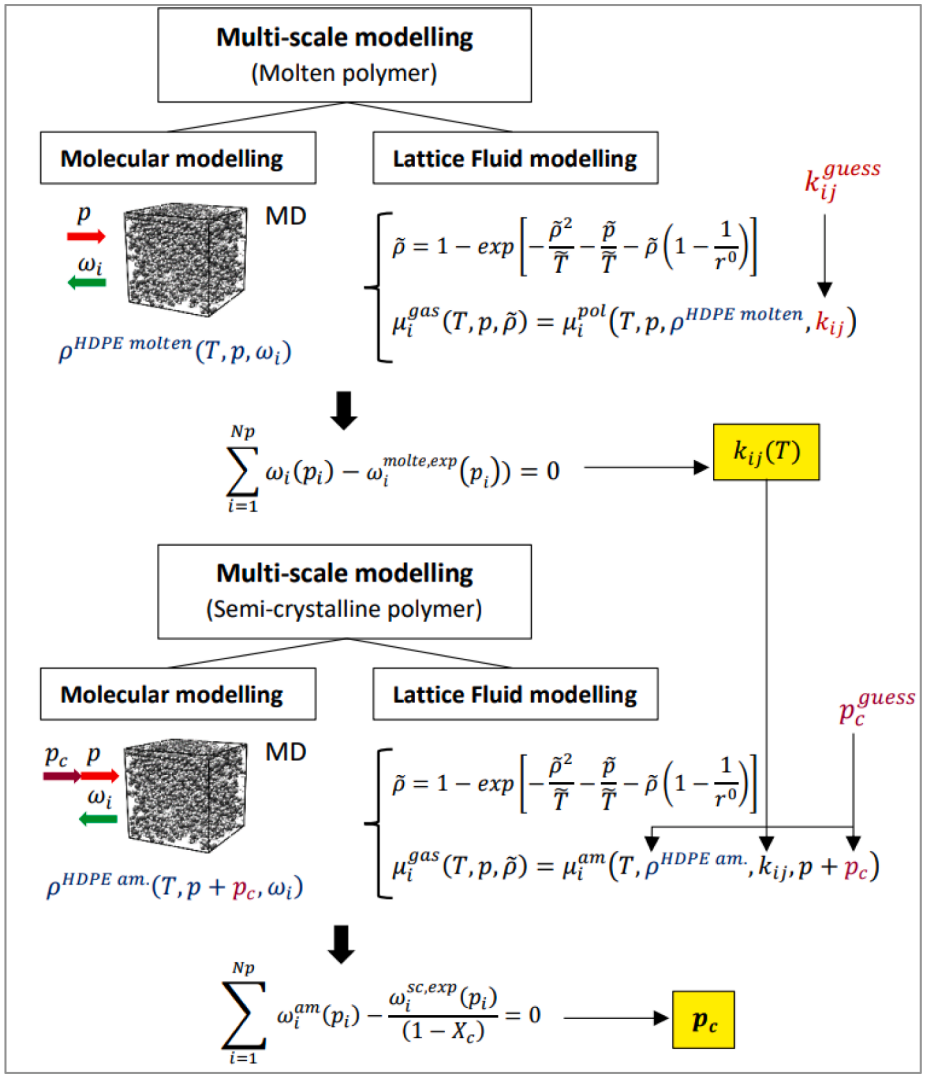

Fig. 2. Multi-scale modeling strategy paradigm: MD simulations + LF theory. 1) Solubility in the molten polymer, $k_{ij}(T)$ relationship. 2) Solubility in the semi-crystalline polymer, p_c parameter.

strategy here presented allows the prediction of gas solubility in semi-crystalline HDPE by coupling the MD simulated amorphous phase density with the Lattice Fluid theory. In particular, the mixture P-V-T data were described with MD simulations, thus establishing a key link between the atomistic and macroscopic scales. The multi-scale modeling paradigm, which is displayed in detail in Fig. 2, consists of two steps. In both stages the density of the pure gas phase $\widetilde{\rho}$ is calculated, as usual, using the LF EoS.

1) MD simulations of the polymer-penetrant mixture above the melting point are used to generate the molten polymer density in mixture, $\rho^{HDPE\ molten}$, that is fed to the LF chemical potential to calculate solubility ω_i^{molten}, which is then fitted to the experimental isotherms $\omega_i^{molten,\ exp}$. This multi-scale model is repeated on at least three experimental solubility isotherms in molten HDPE, to retrieve an expression of the model binary interaction parameter as a function of temperature $k_{ij}(T)$.
2) The $k_{ij}(T)$ expression obtained in 1) is extrapolated below the melting point and fed to the LF model to fit a single experimental solubility isotherm in the semi-crystalline state by adjusting the constraint pressure parameter p_C. At this stage, the MD simulated polymer amorphous density below the melting point, namely, $\rho^{HDPE\ am.}$, is used in the expression of the LF chemical potential.

The modeling paradigm depicted above coincides with the one described by Minelli et al. [30] if the MD simulated mixture density is substituted by the mixture Sanchez-Lacombe EoS. The authors' choice of using MD simulated data will be explained in next chapter.

3. Results

3.1. Pure polymer and pure gasses PVT data modeling

Pure molten HDPE pressure-volume-temperature data were calculated both with atomistic and macroscopic models above and below the melting point and they were reported against the experimental reference [39] in Fig. 3. The fundamental difference between the two approaches is that, while MD simulations are entirely predictive, the LF calculation must be fitted on a certain number of experimental PVT data of the molten polymer to obtain the three characteristic LF parameters. This makes obviously the MD modeling a much more powerful tool to describe the polymer volumetric behavior.

Moreover, as depicted in the graph, even though the chosen molecular structure is a simplified model, having monodispersed chains with lower molecular weight (M_w = 12,406 g/mol) compared to the experimental HDPE sample used as reference for the PVT data (M_w =126,000 g/mol, M_w/M_n = 4.5 [39]), the molten polymer experimental density, thermal expansion, and isothermal compressibility were well represented.

The experimental semi-crystalline polymers' features indeed differ in reason of the specific sample molecular weight distribution, degree of crystallinity, and crystalline morphology. However, for the limited case of gas solubility, which is discussed here, the main variable affecting the latter value by means of the LF theory is the amorphous phase density, which of course can be influenced by the factors previously mentioned. Nevertheless, regarding the molten polymer density, only the molecular weight distribution may cause a substantial discrepancy in reason of the density increasing and asymptotic behavior with the molecular weight [41]. In this context, due to the common high molecular weight exhibited and the presence of non-bulky end-chain groups, the molten densities of HDPE samples having different molecular weight distributions are expected to lie in a narrow region within the value of the plateau. For this reason, the simplified molecular model is believed to be representative not only for the PVT data of the reference HDPE sample previously reported, but also the ones of the several HDPE samples whose experimental solubility isotherms will be used in the testing of the multi-scale modeling.

The readers might have noticed that no molecular simulations of the gasses were carried out in order to validate the force field ability to faithfully reproduce also the pure gasses PVT data. In this context, PCFF

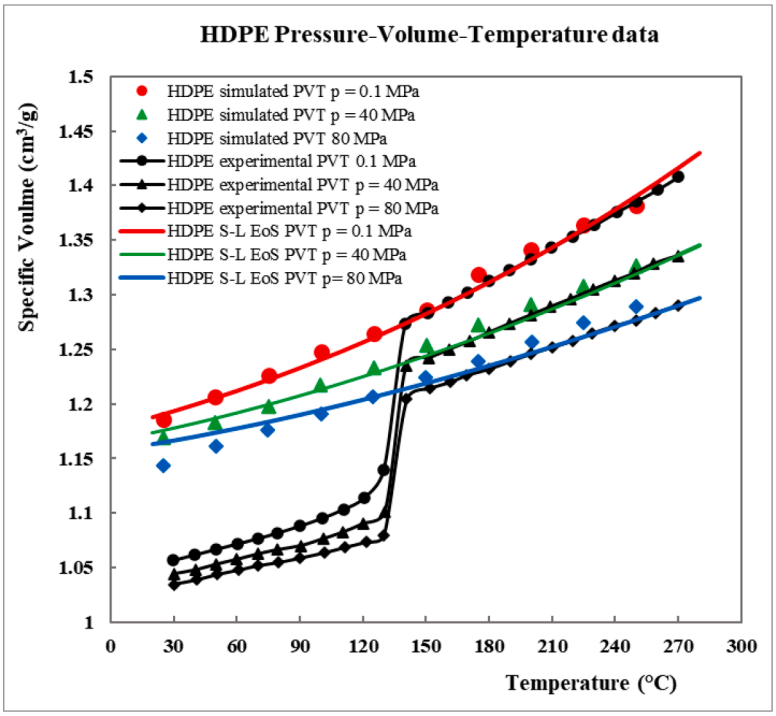

Fig. 3. HDPE Pressure-Volume-Temperature data: Experimental data [39]: 0.1 MPa (black dots), 40 MPa (black triangles), 80 MPa (black diamonds). MD simulated data: 0.1 MPa (red dots), 40 MPa (green triangles), 80 MPa (blue diamonds). Sanchez-Lacombe EoS modeling: 0.1 MPa (red line), 40 MPa (green line), and 80 MPa (blue line).

force field parameters assigned to CO_2 are the same reported in literature as resulting from the optimization of the COMPASS force field, which shares the same functional form of PCFF, and was demonstrated capable of reproducing a series of CO_2 thermophysical properties at normal and critical conditions, including the gas PVT data [42]. Therefore, the PCFF demonstrated ability to describe hydrocarbon structures such as HDPE chains and a polar small molecule like CO_2 led the authors to consider it reliable to model hydrocarbon gasses such as ethylene and propane without any further checks. On the other hand, thermodynamic modeling was carried out for both pure HDPE and gasses. HDPE and penetrants S-L EoS parameters used for the thermodynamic modeling can be found in Table 2.

3.2. Gas-polymer mixture volume modeling

Both the MD and S-L EoS can model the polymer-gas mixture volume, although the EoS needs some additional information, namely the binary interaction parameter. Such a parameter was derived from the fitting of molten solubility isotherms with the fully macroscopic approach proposed by Minelli et al., for each penetrant. For the sake of synthesis, the authors chose to report the comparison of MD and S-L EoS modelled mixture data only for the system $HDPE_{am.}$-CO_2 in Fig. 4. Analogous results for ethylene-$HDPE_{am.}$ and propane-$HDPE_{am}$ systems can be retrieved in Figs. S1 and S2 in the *Supporting Information*. The experimental molten solubility isotherms used in the fitting procedure for the S-L EoS can be found in Refs. [43,44].

The displayed P-V-T data report how the polymer specific volume changes with the penetrant mass fraction at the given temperature and pressure ranges. It is therefore reasonable that with increasing CO_2 concentration a more significant swelling of the amorphous matrix occurs. Someone could argue that, at a fixed temperature and gas pressure, the only consistent penetrant mass fraction is the thermodynamic equilibrium one. For this reason, it is important to clarify that, at this level, MD simulations results and EoS modelled data are intended to provide us just with a comparison of the mapping of the polymer density for several pressures, temperatures, and penetrant mass fractions without any regard for the actual thermodynamic equilibrium. The chemical potentials equalization at the thermodynamic level, coupled with the P-V-T-ω_i relationship, either from S-L mixture EoS or MD simulations results, would instead provide the actual penetrant mass fraction and the corresponding polymer density according to the fully thermodynamic approach or the multi-scale model here presented, respectively.

It is interesting to notice that MD and S-L EoS derived mixture data show a good match and it is worth it to stress that the latter is not provoked by a cross-fitting; the two derivations are in fact uncoupled. MD simulations provide a full prediction of the mixture density, by accounting for the penetrant-polymer interactions which are directly shaped by the force field, whereas the S-L mixture EoS modelled density was derived by prior fitting of the binary interaction parameter relationship with temperature $k_{ij}(T)$ on the experimental solubility data in the molten polymer and not on the MD simulated data themselves. Nevertheless, some deviations are evident at the lowest mass fractions below 70 °C, namely, in the region where experimental solubility isotherms in semi-crystalline HDPE lay. In particular, the EoS provides a systematically higher value of the theoretical amorphous phase specific volume with respect to MD simulations and that in turn would affect the value of the constraint pressure parameter that has to be added to match the experimental solubility. The authors believe that the atomistic model is superior in describing the polymer-gas mixture volume, and literature provides examples of the mismatch between the experimental measured swelling and the one predicted by even advanced equations of state [45]. Hence, we have chosen to rely on MD simulated mixture volumetric data, thus establishing the key link between the microscopic and macroscopic approach.

Rearranging the MD simulated P-V-T simulated data, it was noticed that at any given temperature and pressure the polymer density is, with excellent approximation, a linear function of the penetrant mass fraction, thus, the previously reported P-V-T data were fitted according to the relationship reported in Eq. (12) which is the one that is ultimately fed to the Lattice Fluid model in place of the S-L EoS when calculating the solubility. A visual rendering of the linearity is reported in Fig. S3 in the *Supporting Information* at a temperature equal to 25 °C.

$$\rho_{HDPE_{am.}}(T,p,\omega_i) = \alpha_{sw,i}(T,p)\omega_i + \rho^{\circ}_{HDPE_{am.}}(T,p) \tag{12}$$

Where $\rho^{\circ}_{HDPE_{am.}}$ and $\rho_{HDPE_{am.}}$ are the pure polymer density and in mixture respectively, while $\alpha_{sw,i}$ figures as the polymer dilatation coefficient due to the swelling induced by the penetrant *i*. $\rho^{\circ}_{HDPE_{am.}}$ can be easily retrieved from the pure amorphous HDPE simulated P-V-T data displayed in Fig. 3. whereas the values of the dilatation coefficients $(\alpha_{sw,CO_2}, \alpha_{sw,C_2H_4}, \alpha_{sw,C_3H_8})$ fitted with Eq. (12) are summarized in Table 3.

3.3. Solubility multi-scale modeling results

Having parametrized the relationship reported in Eq. (12), the predictive ability of the multi-scale strategy depicted in Fig. 2 could be finally tested. As already explained, the first part of the model allowed us to retrieve the penetrant-polymer binary interaction parameter relation with temperature. In this framework, the experimental solubility data in the molten polymer that were fitted to retrieve the k_{ij} (T) are the ones already introduced in previous chapter when comparing the S-L EoS prediction with the MD results. Results of the model application to molten solubility isotherms are reported in Fig. 5.

As displayed in the chart, the model gives a good prediction of the solubility in the molten polymer, even though some deviations are evident for CO_2 solubility data; the authors believe that the fitting of the binary interaction parameter is still acceptable, nonetheless.

The found $k_{ij}(T)$ expressions could be readily extrapolated below the melting temperature hence allowing the solubility modeling in the semi-crystalline state as depicted in Figs. 6, 7, and 8 for CO_2, ethylene, and propane respectively. The experimental solubility isotherms used in the modeling are reported in Refs. [15,18,46-49].

The results show that a temperature-independent constraint pressure fitted from a single solubility isotherm of a penetrant can provide reliable predictions at different temperatures as well. The extension of the parameter to different samples of the same polymer also led to excellent results for the case of propane solubility in HDPE; ethylene solubility predictions showed good overall results even though some deviations are evident. However, it is visible that experimental solubility data for ethylene from different references are not consistent with each other; for instance, the fitted solubility isotherm at 60 °C (sample 1) is in between the solubility isotherms at 68 °C and 88 °C of sample 3. Since the provided mass degree of crystallinity are 0.665 and 0.702 respectively, the data location cannot be justified with the idea that a higher crystal content leads to a more pronounced constraint effect. The authors believe, instead, that the uncertainty on the value of the sample degree of crystallinity, which was used to scale the experimental data on the amorphous phase fraction, was the major reason for the data shifting and consequent modest transferability of the fitted parameter to other samples. The most relevant evidence was the dependence of the fitted constraint pressure parameter on the penetrant type. Such a result was

Table 2
Compounds Sanchez-Lacombe parameters used in this work.

Compound	Sanchez-Lacombe EoS parameters		
	T^*(K)	p^*(MPa)	ρ^*(g/cm^3)
HDPE	687.13	396.98	0.8821
CO_2 [38]	341.80	419.90	1.3970
Ethylene	332.27	285.49	0.6272
Propane	354.40	380.18	0.7065

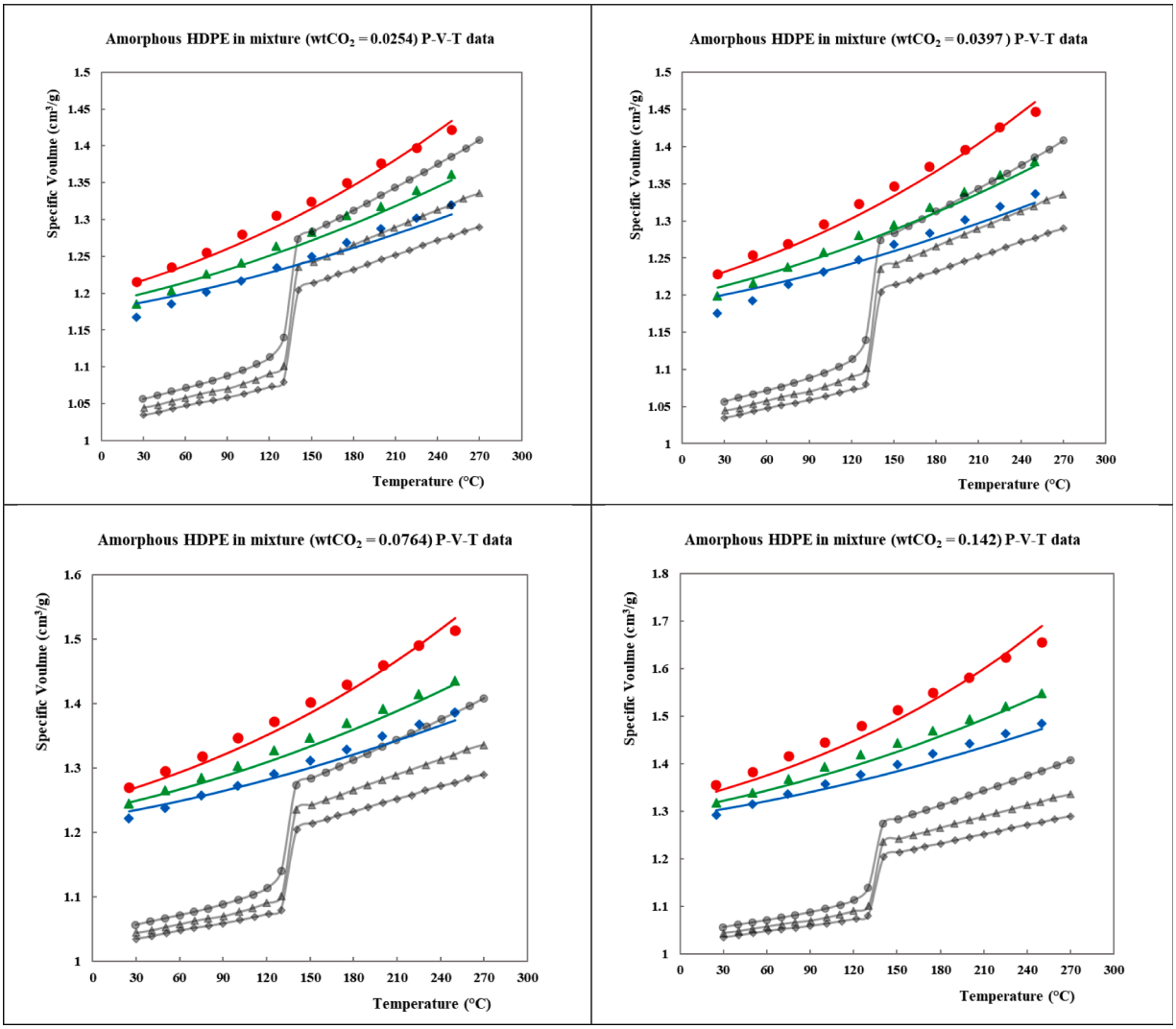

Fig. 4. HDPE $_{am.}$ Pressure-Volume-Temperature data with different mass fractions of CO_2 (wt_{CO_2}=0.0254, 0.0397,0.0764, and 0.142). Pure HDPE experimental P-V-T data: 0.1 MPa (gray dots), 40 MPa (gray triangles), 80 MPa (gray diamonds). HDPE $_{am.}$ simulated P-V-T data at different mass fractions of CO_2: 0.1 MPa (red dots), 40 MPa (green triangles), 80 MPa (blue diamonds). HDPE $_{am.}$ P-V-T data modelled with S-L EoS at different mass fractions of CO_2: 0.1 MPa (red line), 40 MPa (green line), 80 MPa (blue line).

Table 3
HDPE$_{am.}$ dilation coefficients $\alpha_{sw,i}$ with CO_2, ethylene, and propane penetrants fitted from mixture MD simulated P-V-T data using Eq. (12).

	$\alpha_{sw,\ CO_2}$ (g/cm^3)			α_{sw,C_2H_4} (g/cm^3)			α_{sw,C_3H_8} (g/cm^3)		
T (°C)	0.1 MPa	40 MPa	80 MPa	0.1 MPa	40 MPa	80 MPa	0.1 MPa	40 MPa	80 MPa
25	−0.738	−0.702	−0.719	−1.351	−1.284	−0.994	−1.260	−1.169	−1.188
50	−0.747	−0.715	−0.719	−1.354	−1.297	−0.978	−1.252	−1.172	−1.176
75	−0.774	−0.736	−0.717	−1.365	−1.308	−0.988	−1.265	−1.176	−1.176
100	−0.773	−0.740	−0.729	−1.369	−1.324	−0.988	−1.251	−1.178	−1.183
125	−0.799	−0.749	−0.722	−1.422	−1.318	−0.971	−1.246	−1.183	−1.160
150	−0.819	−0.743	−0.721	−1.430	−1.329	−0.956	−1.258	−1.158	−1.149
175	−0.800	−0.737	−0.724	−1.424	−1.328	−0.958	−1.259	−1.153	−1.159
200	−0.803	−0.751	−0.718	−1.436	−1.308	−0.940	−1.275	−1.140	−1.138
225	−0.837	−0.755	−0.719	−1.459	−1.319	−0.943	−1.301	−1.134	−1.122
250	−0.846	−0.757	−0.722	−1.478	−1.338	−0.944	−1.283	−1.116	−1.106

not expected since, in principle, the entity of the physical constraint was thought to be a solely material property. The mismatch is believed to be related to the model sensitivity on the value of the binary interaction parameter and the extrapolation of the latter across temperature intervals larger than 100 °C.

In order to evaluate the efficiency of the developed model, one should make a comparison against the already existing fully thermodynamic approach with adjustable constraint pressure (Minelli et al. [30].) and the predictive thermodynamic model with constraint pressure from continuum mechanics (Fischlschweiger et al. [31]). While in the first approach the constraint pressure is simply treated as an adjustable parameter, in the latter the constraint pressure felt by the

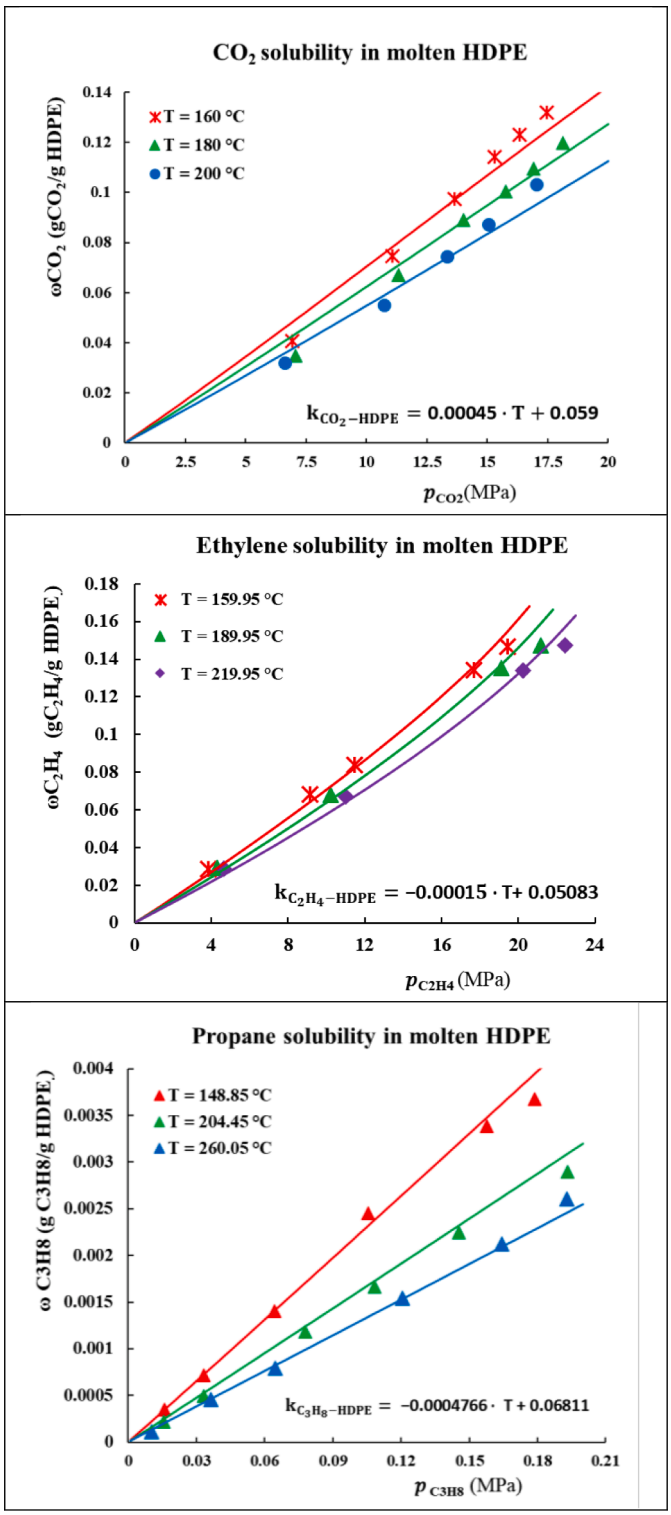

Fig. 5. Multi-scale modeling of CO_2, ethylene, and propane solubility in molten HDPE. Experimental data points from [43,44] & Multi-scale model prediction (continuous lines).

amorphous phase (the '*Eigen pressure*' in the original article) can be predicted by the relationship suggested by the authors:

$$p_c = \left(K\left(\frac{\Delta\tilde{v}}{\tilde{v}}\right) + 2.5G\right)X_c \tag{13}$$

where $\left(\frac{\Delta\tilde{v}}{\tilde{v}}\right)$ is the relative volume change of the mixture in the amorphous phase triggered by the solute sorption, the reference state $\tilde{v}$ is the volume of the pure amorphous polymer, K and G are the material bulk and shear modulus respectively. A correct application of the model requires reliable values of mechanical parameters K and G, obtained on the same samples on which solubility isotherms are performed. Indeed, it is well known that different HDPE samples may differ for a series of features such as the molecular weight distribution, degree of branching, degree of crystallinity, and crystalline morphology. In addition, such properties are known to have a non-negligible temperature and time dependence. A fair comparison between the latter model and the models treating the constraint pressure as an adjustable parameter was thus not possible here, because the HDPE moduli K and G found in literature [50], were not relative to the sample used for the solubility tests, and varied over a very broad range (G = 100–1000 MPa). In Table 4 we thus reported and compared only the parameters obtained by the thermodynamic model of Minelli et al. [30] with the multi-scale model of this work.

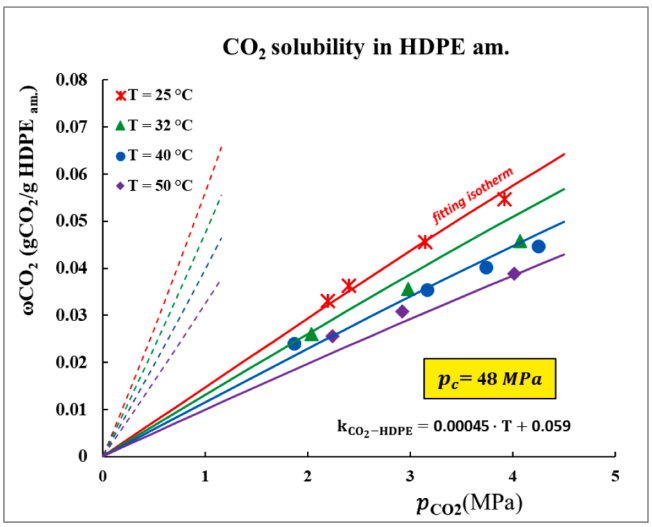

Fig. 6. Multi-scale modeling of CO_2 solubility in semi-crystalline HDPE. Experimental solubility data points [46]: T = 25 °C (red crosses), T = 32 °C (green triangles), T = 40 °C (blue dots), T = 50 °C (violet diamonds). Bare Lattice Fluid model prediction with zero constraint pressure: T = 25 °C (red dashed line), T = 32 °C (green dashed line), T = 40 °C (blue dashed line), T = 50 °C (violet dashed line). Multi-scale model prediction with constant p_c and k_{ij}(T) from molten solubility isotherms: T = 25 °C (red continuous line), T = 32 °C (green continuous line), T = 40 °C (blue continuous line), T = 50 °C (violet continuous line).

The multi-scale and the fully thermodynamic models are comparable in terms of outputs and parameters, even though the fully thermodynamic one requires slightly higher values of the constraint pressure, due to the higher aforementioned mixture volume estimated at low temperatures by the EoS.

Nevertheless, the predictive potential of the MD simulations is much higher. Indeed, the atomistic model provides a pure prediction of the polymer and polymer-gas mixture volume at different pressures, temperatures, and compositions without any adjustable pure component or mixture parameter. The reliability of MD predictions was successfully tested on experimental data for the pure polymer PVT data available in the literature. For the mixture volumetric behavior, there were no experimental swelling data available for this gas-polymer system to validate the simulations. However, an indirect proof of the accuracy of the volume calculated with MD model in the binary case comes from its agreement with the one given by the macroscopic approach, i.e., the S-L EoS, which, unlike MD simulations, needs to be informed by experimental solubility data on the specific gas-polymer mixture, which provide the k_{ij}, nonetheless. Moreover, compared to a fully molecular derivation of the solubility in semi-crystalline polymers, such as the

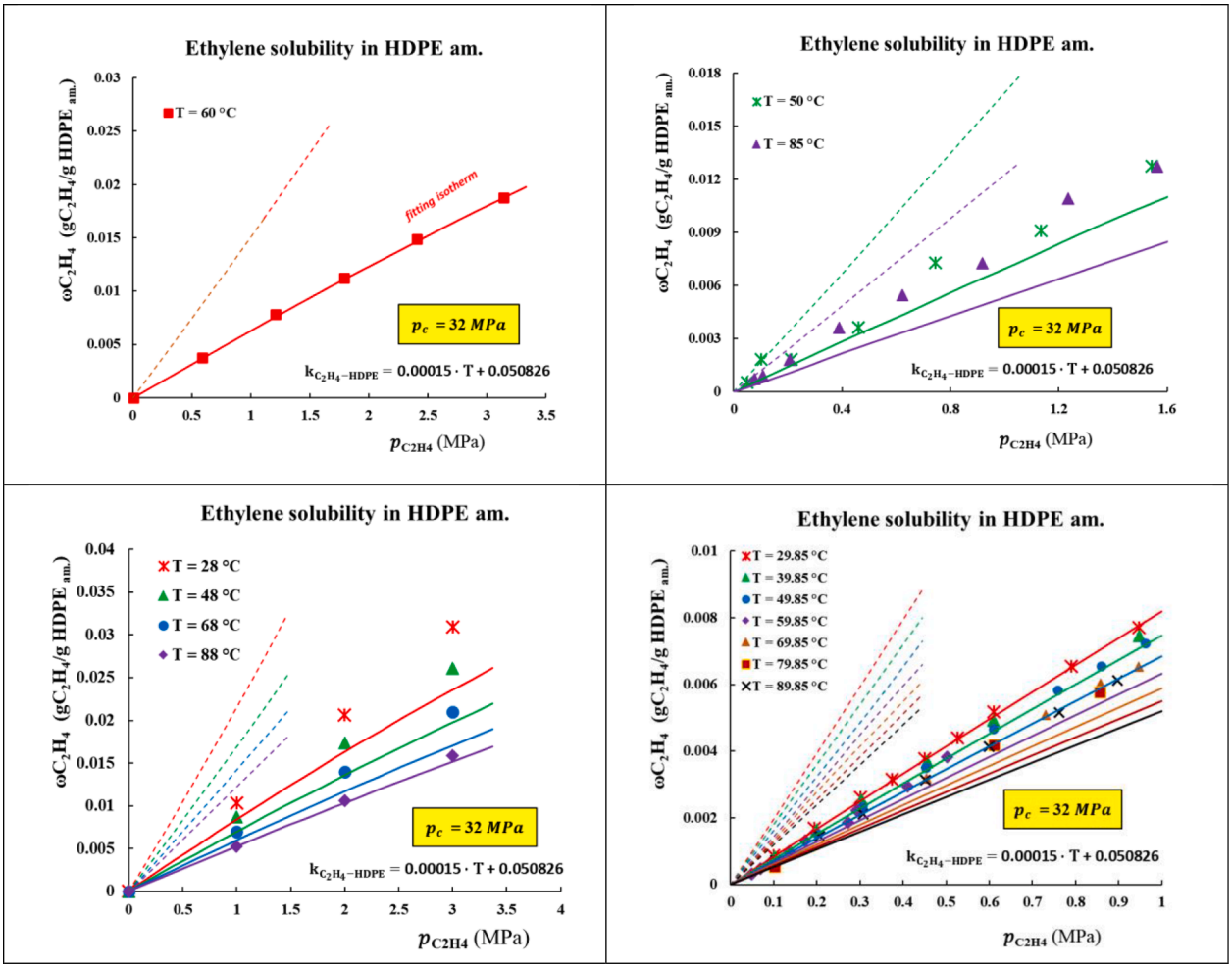

Fig. 7. Multi-scale modeling of Ethylene solubility in different semi-crystalline HDPE samples (sample 1: up-left, sample 2: up-right, sample 3: bottom-left, sample 4: bottom-right). Experimental solubility data points from Refs. [18,47–49]. Bare Lattice Fluid model prediction with zero constraint pressure (dashed lines). Multi-scale model prediction with constant p_c and $k_{ij}(T)$ from molten solubility isotherms (continuous lines).

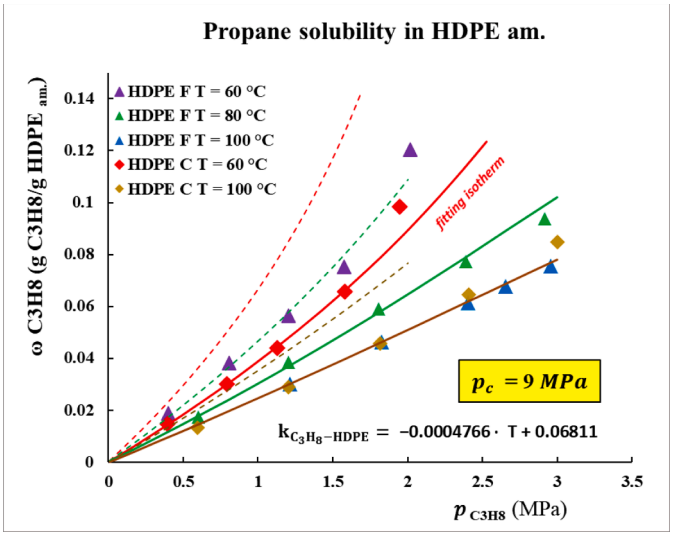

Fig. 8. Multi-scale modeling of Propane solubility in two different semi-crystalline HDPE samples. Experimental solubility data points from [15]. Bare Lattice Fluid model prediction with zero constraint pressure (dashed lines). Multi-scale model prediction with constant p_c and $k_{ij}(T)$ from molten solubility isotherms (continuous line).

Table 4
Comparison between the parameters of the fully thermodynamic model with adjustable constraint pressure and the multi-scale model proposed in this work.

	HDPE-CO_2	HDPE-ethylene	HDPE-propane
Thermodynamic model, Minelli et al. [30].			
$k_{ij}(T)$ (T in °C)	0.0004·T+0.04667	0.000333·T+0.04331	0.000396·T+0.0519
p_c (MPa)	58	42	10
Multi-scale model (this work)			
$k_{ij}(T)$ (T in °C)	0.00045·T+0.059	0.00015·T+0.0508	−0.000477·T+0.0681
p_c (MPa)	48	32	9

work carried out by Memari et al. [27]., the multi-scale strategy still benefits from the accuracy provided by the atomistic description in the representation of the polymer volume at various temperatures, pressures, and concentrations of penetrant, but without relying on time-consuming simulations of the phase equilibrium, which, instead, is performed at thermodynamic level.

4. Conclusions

A multi-scale modeling strategy is presented to evaluate fluid solubility isotherms in semi-crystalline polymers.

The results of the multi-scale model are consistent with the ones

provided by a previously proposed, solely macroscopic approach, but, in addition, have demonstrated the potential of relying on less experimental data.

A temperature-independent constraint pressure fitted from a single solubility isotherm of a penetrant can provide reliable predictions at different temperatures and on different polymer samples.

The reliability of the multi-scale coupling presented in this work is promising for the advancement of multi-scale modeling of semi-crystalline materials.

In the next step we aim to obtain quantitative information on the constrained state of the amorphous state with an explicit MD simulation of the crystal-amorphous interface.

CRediT authorship contribution statement

Omar Atiq: Conceptualization, Methodology, Software, Formal analysis, Data curation, Visualization, Writing – original draft, Writing – review & editing. **Eleonora Ricci:** Conceptualization, Methodology, Software, Formal analysis, Data curation, Visualization, Writing – review & editing. **Marco Giacinti Baschetti:** Conceptualization, Writing – review & editing, Supervision, Project administration, Funding acquisition. **Maria Grazia De Angelis:** Conceptualization, Writing – review & editing, Supervision, Project administration, Funding acquisition.

Declaration of Competing Interest

The authors declare that they have no known competing financial interests or personal relationships that could have appeared to influence the work reported in this paper.

Data availability

Data will be made available on request.

Acknowledgments

This research forms part of the research program of DPI, project 844: *Modelling and Design of Multiphase Polymeric Materials for High Performance Applications Across Multiple Scales (MumPol)*.

We acknowledge the CINECA award under the ISCRA initiative, for the availability of high- performance computing resources and support: project IsC92_GS-SCP.

The financial contribution of the Italian National Ministry of University and Research is acknowledged for the PhD scholarship of Mr. Omar Atiq.

Supplementary materials

Supplementary material associated with this article can be found, in the online version, at doi:10.1016/j.fluid.2023.113798.

References

[1] W. Cao, K. Wang, Q. Zhang, R. Du, Q. Fu, The hierarchy structure and orientation of high density polyethylene obtained via dynamic packing injection molding, Polymer (Guildf) 47 (2006) 6857–6867, https://doi.org/10.1016/j.polymer.2006.07.037.

[2] H. Teng, Y. Shi, X. Jin, Inter-spherulite boundary structure in bulk-crystallized polyethylenes directly observed by atomic force microscopy, Polym. J. 35 (2003) 436–439, https://doi.org/10.1295/polymj.35.436.

[3] C. Zhang, L. Lu, W. Li, L. Li, C. Zhou, Effects of crystallization temperature and spherulite size on cracking behavior of semi-crystalline polymers, Polym. Bull. 73 (2016) 2961–2972, https://doi.org/10.1007/s00289-016-1634-2.

[4] E. Giannetti, Featured Article Semi-crystalline fluorinated polymers, Polym. Int. 50 (2001) 10–26.

[5] N. Jia, V.A. Kagan. Mechanical Performance of Polyamides with Influence of Moisture and Temperature - Accurate Evaluation and Better Understanding, Plastics Failure Analysis and Prevention, 2001, https://doi.org/10.1016/b978-188420792-1.50014-7.

[6] E.N. Brown, D.M. Dattelbaum, The role of crystalline phase on fracture and microstructure evolution of polytetrafluoroethylene (PTFE), Polymer (Guildf) 46 (2005) 3056–3068, https://doi.org/10.1016/j.polymer.2005.01.061.

[7] Q. Lozay, Q. Beuguel, N. Follain, L. Lebrun, A. Guinault, G. Miquelard-Garnier, S. Tencé-Girault, C. Sollogoub, E. Dargent, S. Marais, Structural and barrier properties of compatibilized PE/PA6 multinanolayer films, Membranes (Basel) 11 (2021) 1–22, https://doi.org/10.3390/membranes11020075.

[8] Y. Sun, H. Lv, W. Zhou, C. Zhang, Research on hydrogen permeability of polyamide 6 as the liner material for type IV hydrogen storage tank, Int. J. Hydrogen Energy 45 (2020) 24980–24990, https://doi.org/10.1016/j.ijhydene.2020.06.174.

[9] S. Singha, M.S. Hedenqvist, A review on barrier properties of poly(lactic Acid)/clay nanocomposites, Polymers (Basel) 12 (2020), https://doi.org/10.3390/POLYM12051095.

[10] F. Wu, M. Misra, A.K. Mohanty, Challenges and new opportunities on barrier performance of biodegradable polymers for sustainable packaging, Prog. Polym. Sci. 117 (2021), 101395, https://doi.org/10.1016/j.progpolymsci.2021.101395.

[11] L. Ansaloni, B. Alcock, T.A. Peters, Effects of CO2 on polymeric materials in the CO2 transport chain: a review, Int. J. Greenh. Gas Control. 94 (2020), 102930, https://doi.org/10.1016/j.ijggc.2019.102930.

[12] H. Fujiwara, H. Ono, K. Onoue, S. Nishimura, High-pressure gaseous hydrogen permeation test method -property of polymeric materials for high-pressure hydrogen devices (1), Int. J. Hydrogen Energy 45 (2020) 29082–29094, https://doi.org/10.1016/j.ijhydene.2020.07.215.

[13] J.G. Wijmans, R.W. Baker, The solution-diffusion model: a review, J. Membr. Sci. 107 (1995) 1–21, https://doi.org/10.1016/S0166-4115(08)60038-2.

[14] J. Chmelař, R. Pokorný, P. Schneider, K. Smolná, P. Bělský, J. Kosek, Free and constrained amorphous phases in polyethylene: interpretation of 1H NMR and SAXS data over a broad range of crystallinity, Polymer (Guildf) 58 (2015) 189–198, https://doi.org/10.1016/j.polymer.2014.12.036.

[15] J. Chmelař, K. Haškovcová, M. Podivinská, J. Kosek, Equilibrium sorption of propane and 1-hexene in polyethylene: experiments and perturbed-chain statistical associating fluid theory simulations, Ind. Eng. Chem. Res. 56 (2017) 6820–6826, https://doi.org/10.1021/acs.iecr.7b00572.

[16] J. Lin, S. Shenogin, S. Nazarenko, Oxygen solubility and specific volume of rigid amorphous fraction in semicrystalline poly(ethylene terephthalate), Polymer (Guildf) 43 (2002) 4733–4743, https://doi.org/10.1016/S0032-3861(02)00278-1.

[17] D.R. Sturm, K.J. Caputo, S. Liu, R.P. Danner, Solubility of solvents in polyethylene below the melt temperature, Fluid Phase Equilib. 470 (2018) 68–74, https://doi.org/10.1016/j.fluid.2017.09.004.

[18] B.J. Savatsky, J.A. Moebus, B.R. Greenhalgh, Parameterization of models for vapor solubility in semicrystalline polyethylene, Macromol. React. Eng. 13 (2019) 1–17, https://doi.org/10.1002/mren.201900003.

[19] M. Minelli, M.G. Baschetti, F. Doghieri, A comprehensive model for mass transport properties in nanocomposites, J. Membr. Sci. 381 (2011) 10–20, https://doi.org/10.1016/j.memsci.2011.06.036.

[20] R. Pokorny, L. Seda, Z. Grof, H. Hajova, J. Kosek, Diffusion in semi-crystalline polymers, in: 19th European Symposium on Computer Aided Process Engineering – ESCAPE19, Elsevier B.V., 2009, https://doi.org/10.1016/S1570-7946(09)70160-9.

[21] X. Chen, T.D. Papathanasiou, Barrier properties of flake-filled membranes: review and numerical evaluation, J. Plast. Film Sheeting 23 (2007) 319–345, https://doi.org/10.1177/8756087907088437.

[22] R.H.B. Bouma, A. Checchetti, G. Chidichimo, E. Drioli, Permeation through a heterogeneous membrane: the effect of the dispersed phase, J. Membr. Sci. 128 (1997) 141–149, https://doi.org/10.1016/S0376-7388(96)00303-1.

[23] S. Zid, M. Zinet, E. Espuche, Modeling diffusion mass transport in multiphase polymer systems for gas barrier applications: a review, J. Polym. Sci. B Polym. Phys. 56 (2018) 621–639, https://doi.org/10.1002/polb.24574.

[24] O. Atiq, E. Ricci, M.G. Baschetti, M.G. de Angelis, Modelling solubility in semi-crystalline polymers: a critical comparative review, Fluid Phase Equilib. 556 (2022), 113412, https://doi.org/10.1016/j.fluid.2022.113412.

[25] M.A. Bashir, M.A. haj Ali, V. Kanellopoulos, J. Seppälä, Combined EoS and elastic constraints models to predict thermodynamic properties for systems involving semi-crystalline polyolefins, Fluid Phase Equilib. 388 (2015) 107–117, https://doi.org/10.1016/j.fluid.2014.12.046.

[26] A.B. Michaels, R.W. Hausslein, Elastic factors controlling sorption and transport properties of polyethylene, J. Polym. Sci. C Polym. Symp. 10 (1965) 61–86, https://doi.org/10.1002/polc.5070100107.

[27] P. Memari, V. Lachet, B. Rousseau, Molecular simulations of the solubility of gases in polyethylene below its melting temperature, Polymer (Guildf) 51 (2010) 4978–4984, https://doi.org/10.1016/j.polymer.2010.08.020.

[28] P. Memari, V. Lachet, M.H. Klopffer, B. Flaconnèche, B. Rousseau, Gas mixture solubilities in polyethylene below its melting temperature: experimental and molecular simulation studies, J. Membr. Sci. 390–391 (2012) 194–200, https://doi.org/10.1016/j.memsci.2011.11.035.

[29] I.C. Sanchez, R.H. Lacombe, Statistical thermodynamics of polymer solutions, Macromolecules 11 (1978) 1145–1156, https://doi.org/10.1021/ma60066a017.

[30] M. Minelli, M.G. De Angelis, An equation of state (EoS) based model for the fluid solubility in semicrystalline polymers, Fluid Phase Equilib. 367 (2014) 173–181, https://doi.org/10.1016/j.fluid.2014.01.024.

[31] M. Fischlschweiger, A. Danzer, S. Enders, Predicting gas solubility in semi-crystalline polymer solvent systems by consistent coupling of Sanchez-Lacombe EOS with a continuum mechanics approach, Fluid Phase Equilib. 506 (2020), 112379, https://doi.org/10.1016/j.fluid.2019.112379.

[32] Biosym Technologies inc, PCFF force field, (1991). https://git.ecdf.ed.ac.uk/multiscale/lammps/-/blob/5196fa37e072c68db9689f0228f9858bb18385b2/tools/msi2lmp/frc_files/pcff.frc.
[33] A.P. Thompson, H.M. Aktulga, R. Berger, D.S. Bolintineanu, W.M. Brown, P. S. Crozier, J. Pieter, A. Kohlmeyer, S.G. Moore, T. Dac, R. Shan, M.J. Stevens, J. Tranchida, C. Trott, S.J. Plimpton, LAMMPS—a flexible simulation tool for particle-based materials modeling at the atomic, meso, and continuum scales ✩, ✩✩, Comput. Phys. Commun. 271 (2022), 108171 https://doi.org/10.1016/j.cpc.2021.108171.
[34] E.B. Wilson, J.C. Decius, P.C. Cross. Molecular Vibrations: The Theory of Infrared and Raman Vibrational Spectra, Dover Books on Chemistry, 1980. https://www.perlego.com/book/110629/molecular-vibrations-the-theory-of-infrared-and-raman-vibrational-spectra-pdf.
[35] J.R. Maple, M.-.J Hwang, T.P. Stockfisch, U. Dinur, M. Waldman, C.S. Ewig, A. T. Hagler, Derivation of class II force fields. I. Methodology and quantum force field for the alkyl functional group and alkane molecules, J. Comput. Chem. 15 (1994) 162–182, https://doi.org/10.1002/jcc.540150207.
[36] Hockney, R.W., Eastwood, J.W. Computer Simulation Using Particles, 1989. doi:10.1201/9780367806934.
[37] I.C. Sanchez, R.H. Lacombe, Statistical thermodynamics of polymer solutions, Macomolecules 11 (1978) 1145–1156.
[38] K. Von Konigslow, C.B. Park, R.B. Thompson, Evaluating characteristic parameters for carbon dioxide in the Sanchez-Lacombe equation of state, J. Chem. Eng. Data 62 (2017) 585–595, https://doi.org/10.1021/acs.jced.6b00743.
[39] D. Walsh, P. Zoller. Standard Pressure-Volume-Temperature Data for Polymers, 1st ed., CRC Press, 1995, ISBN 1566763282.
[40] R.H. Perry, D.W. Green. Thermodynamic Properties, in: Perry's Chem. Eng. Handb, 8th ed., McGraw-Hill Education, 2007, ISBN 0071422943.
[41] M.A.F. Afzal, C. Cheng, J. Hachmann, Combining first-principles and data modeling for the accurate prediction of the refractive index of organic polymers, J. Chem. Phys. 148 (2018) 241712, https://doi.org/10.1063/1.5007873.
[42] S. Wang, K. Hou, H. Heinz, Accurate and compatible force fields for molecular oxygen, nitrogen, and hydrogen to simulate gases, electrolytes, and heterogeneous interfaces, J. Chem. Theory Comput. 17 (2021) 5198–5213, https://doi.org/10.1021/acs.jctc.0c01132.
[43] Y. Sato, K. Fujiwara, T. Takikawa, S. Sumarno, S. Takishima, H. Masuoka, Solubilities and diffusion coefficients of carbon dioxide and nitrogen in polypropylene, high-density polyethylene, and polystyrene under high pressures and temperatures, Fluid Phase Equilib 162 (1999) 261–276, https://doi.org/10.1016/S0378-3812(99)00217-4.
[44] S.K. Maity, Correlation of solubility of single gases/hydrocarbons in polyethylene using PC-SAFT, Asia Pac. J. Chem. Eng. (2011). 10.1002/apj.574.
[45] M. Podivinská, K. Jindrová, J. Chmelař, J. Kosek, Swelling of polyethylene particles and its relation to sorption equilibria under gas-phase polymerization conditions, J. Appl. Polym. Sci. 134 (2017) 1–7, https://doi.org/10.1002/app.45035.
[46] N. Von Solms, J.K. Nielsen, O. Hassager, A. Rubin, A.Y. Dandekar, S.I. Andersen, E. H. Stenby, Direct measurement of gas solubilities in polymers with a high-pressure microbalance, J. Appl. Polym. Sci. 91 (2004) 1476–1488, https://doi.org/10.1002/app.13371.
[47] J. Chmelař, K. Smolná, K. Haškovcová, M. Podivinská, J. Maršálek, J. Kosek, Equilibrium sorption of ethylene in polyethylene: experimental study and PC-SAFT simulations, Polymer (Guildf) 59 (2015) 270–277, https://doi.org/10.1016/j.polymer.2015.01.012.
[48] Moore, S.J., Wanke, S.E. Solubility of ethylene , 1-butene and 1-hexene in polyethylenes, 56 (2001) 4121–4129.
[49] J. Sun, H. Wang, M. Chen, J. Ye, B. Jiang, J. Wang, Y. Yang, C. Ren, Solubility measurement of hydrogen, ethylene, and 1-hexene in polyethylene films through an intelligent gravimetric analyzer, J. Appl. Polym. Sci. 134 (2017) 1–7, https://doi.org/10.1002/app.44507.
[50] D.W. Van Krevelen, K. Te Nijenhuis, Mechanical properties of solid polymers, in: Prop. Polym, Elsevier, 2009, ISBN 9780444596123, pp. 392–396.